INTERNATIONAL JOURNAL FOR NUMERICAL METHODS IN FLUIDS
Int. J. Numer. Meth. Fluids 2003; **42**:527–548 (DOI: 10.1002/fld.530)

Numerical simulation of the unsteady behaviour of cavitating flows

O. Coutier-Delgosha[1,*,†,‡], J. L. Reboud[1,§,¶] and Y. Delannoy[2,‖]

[1] *LEGI/INPG, BP 53, 38041 Grenoble cedex 9, France*
[2] *EPM-MADYLAM, 38041 Grenoble cedex 9, France*

SUMMARY

A 2D numerical model is proposed to simulate unsteady cavitating flows. The Reynolds-averaged Navier–Stokes equations are solved for the mixture of liquid and vapour, which is considered as a single fluid with variable density. The vapourization and condensation processes are controlled by a barotropic state law that relates the fluid density to the pressure variations. The numerical resolution is a pressure-correction method derived from the SIMPLE algorithm, with a finite volume discretization. The standard scheme is slightly modified to take into account the cavitation phenomenon.

That numerical model is used to calculate unsteady cavitating flows in two Venturi type sections. The choice of the turbulence model is discussed, and the standard RNG k–ε model is found to lead to non-physical stable cavities. A modified k–ε model is proposed to improve the simulation. The influence of numerical and physical parameters is presented, and the numerical results are compared to previous experimental observations and measurements. The proposed model seems to describe the unsteady cavitation behaviour in 2D geometries well. Copyright © 2003 John Wiley & Sons, Ltd.

KEY WORDS: cavitation; two-phase flow; unsteady flow; turbomachinery; barotropic state law; pressure correction method

1. INTRODUCTION

Cavitation is the vapourization of a liquid when the static pressure decreases below its vapour pressure. This phenomenon usually arises in flows around solid bodies and it strongly affects the flow field and the neighbouring structures. In hydraulic machines, for example, several low-pressure areas (suction side leading edge of the blades, tip leakage, separated flows near

* Correspondence to: O. Coutier-Delgosha, ENSTA UME/DFA, chemin de la Hunière, 91761 Palaiseau cedex, France.
† E-mail: coutier@enstay.ensta.fr
‡ Now at ENSTA UME/DFA, chemin de la Hunière, 91761 Palaiseau cedex, France.
§ E-mail: reboud@enise.fr
¶ Now at ENISE - LTDS, 58 rue J. Parot, 42023 St Etienne cedex 2, France.
‖ E-mail: delannoy@hmg.inpg.fr

Contract grant/sponsor: French Space Agency (CNES)

Received 1 September 2001
Revised 2 January 2003

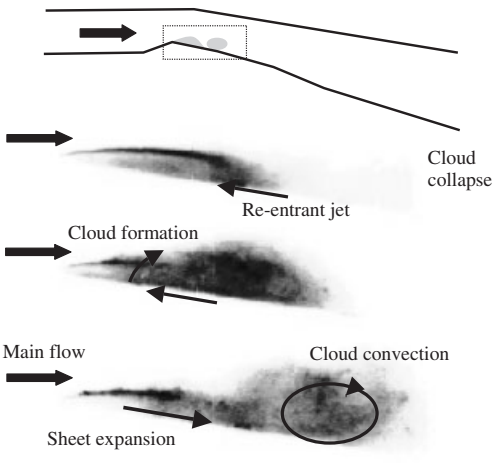

Figure 1. Unsteady cavitation behaviour in a venturi type duct: 3 different stages of cloud shedding process (view from Reference [1]).

the shroud) are susceptible to cavitation. Apparition of vapour induces modifications of the blades load, and strong forces acting on the pump components. If the vapour/liquid structures grow significantly, they can lead to substantial performance losses. The collapse of the vapour structures is also associated with noise and erosion, resulting in supplementary maintenance operations. These effects mainly depend on the time-averaged shape and location of the two-phase structures.

Moreover, the shape and volume of these vapour inclusions usually fluctuate in time. This unstable behaviour is directly associated with the perturbations occurring in pumps, such as vibrations, flow rate fluctuations and compressibility effects. Therefore, understanding of unsteady two-phase flow structure of cavitation is important for the design of turbomachinery and hydraulic plants.

According to experimental observations, cavitation sheets that appear on solid bodies are very complex: their structure (smooth or rough, stable or unstable) depends on the shape and roughness of the surface (Venturi, hydrofoil, blade) and on the operating conditions. A stable cavity is characterized by a length almost constant in time, although the closure region always fluctuates. On the contrary, an unstable cavitation sheet often adopts a cyclic behaviour (Figure 1): the cavity attached to the solid body grows up to the generation of a re-entrant jet. This one is mainly composed of liquid, which flows upstream along the solid surface and leads to the break-off of the downstream part of the cavity. The resulting cloud of vapour is then carried away by the main stream, until it enters a higher-pressure zone and collapses. The remaining part of the attached cavitation sheet re-expands and a new cycle starts.

Whatever the case—stable or unstable—the closure region of the cavity is a very complex two-phase structure, which is always unsteady at some scale.

Several physical and numerical models have been developed to investigate stable cavities. They usually consist of describing the vapour/liquid interface as a stream sheet at constant static pressure equal to the vapour pressure. The shape is obtained by solving an inverse problem. Previous numerical and theoretical models of cavitating flows on pumps or propeller

blades proposed for example by Kueny *et al.* [2], Kinnas and Fine [3], Von Kaenel *et al.* [4], Peallat and Pellone [5] are based on this kind of numerical simulation of steady cavitation sheets. In a time-accurate formulation, this type of model is able to simulate the early stage of the re-entrant jet formation [6, 7], but not the complete vapour cloud shedding process, since it becomes quite difficult to manage several vapour/liquid interfaces inside the flow field. Therefore, these models predict only the mean shape of cavities and do not adapt to unsteady cavitation.

To simulate unsteady phenomena, such as pulsating cavities and vapour cloud shedding, an alternative approach is to model the cavitating liquid as a homogeneous two-phase mixture of liquid and vapour. A classical assumption in this case is to neglect the possible slip between the two phases, which leads to a single-phase fluid whose density may vary over a large range from pure liquid to pure vapour. The main numerical problem in multidimensional simulations is the simultaneous treatment of two very different flow conditions: two almost incompressible ones (pure liquid and pure vapour), and a highly compressible one in the transition between vapour and liquid. Most of the methods have serious difficulties when the ratio ρ_v/ρ_l is lowered. This approach has been investigated in different ways:

Delannoy and Kueny [8] proposed a formulation that strongly links the mixture density to the static pressure: they use a barotropic law $\rho(P)$, which describes the mixture density both in the incompressible parts of the flow field and in the transition zone. This kind of model has been applied recently by Merkle *et al.* [9], Song *et al.* [10], and Hoeijmakers *et al.* [32]. They obtained satisfactory results for various types of geometry, such as Venturi type ducts or hydrofoils.

Kubota *et al.* [11] relate the density evolution to the motion of bubbles in the flow. A given number of bubbles are settled at the inlet, and their evolution is governed by the Rayleigh–Plesset equation according to the pressure field. It is assumed that the bubbles are spherical, and remain not too close from each other. The void fraction is thus theoretically limited to a small value, much smaller than the experimental ones. That approach has been widely developed since that time, in particular by Chen and Heister [12], Grogger and Alajbegovic [13].

Merkle *et al.* [9] and Kunz *et al.* [14] recently proposed a third development: they consider two mass balance equations, one for liquid and one for vapour, instead of a single one for the mixture. A vapourization/condensation term in these equations controls the mass transfer between the two phases. The results are quite similar to the previous ones [9], but this method has the advantage that it can take into account other non-condensed phases and the time influence on the mass transfer phenomena.

Nevertheless, very few authors have obtained a complete description of the pulsating behaviour of the cavitation sheet. The formation of the reverse flow along the surface, resulting in the cavity break-off, and the convection of the cloud of vapour downstream, remain very difficult to simulate.

Mainly two numerical methods have been developed to simulate unsteady cavitation. The major difficulty lies in the requirement to compute an unsteady flow field of quasi-incompressible fluids (pure liquid or vapour) in association with a very high compressibility in the phase change regions.

The first method is based on the adaptation of compressible time-marching algorithms to low Mach numbers. This kind of resolution was originally devoted to highly compressible flows. In the case of low-compressible or incompressible simulations, its efficiency was originally observed to decrease dramatically. This well-known problem has been addressed by many

authors [15, 31] and solved by introducing a preconditioner. It consists in multiplying the pseudo-time derivatives by a preconditioning matrix that modifies the equations and accelerates the convergence, without altering the result accuracy provided each time step is correctly converged. Merkle *et al.* [1993] implemented it in an implicit algorithm, and they obtained satisfactory results, either with a barotropic law or a two mass equations model. The rate ρ_v/ρ_l was lowered until 0.01. Hoeijmakers *et al.* (1998) presented a similar development with a simpler preconditioner applied on an explicit algorithm: ρ_v/ρ_l could not be decreased in their case lower than 0.05. Kunz *et al.* [14] recently presented some promising results obtained with this algorithm, using a three-fluid method based on two mass transfer equations and including the presence of a non-condensable gas.

An alternative numerical treatment, particularly well adapted to incompressible fluids computations, is the pressure correction method, based on the SIMPLE scheme initially proposed by Patankar [16]. Delannoy and Kueny [8] adapted this algorithm to cavitation by considering the mass equation as a transport equation for density, which depends on the pressure through a barotropic state law. This method, first developed for inviscid fluids, considers a physical sound celerity in the vapour/liquid transition and, thus, captures the very strong density gradient in the mixture.

This paper presents a two-dimensional code performing unsteady cavitating simulations. The time dependent Reynolds-averaged Navier–Stokes equations are solved on structured meshes, in association with the cavitation model initially developed by Delannoy and Kueny [8]. Several physical modifications have been investigated by Reboud and Delannoy [17], Reboud *et al.* [1], Coutier-Delgosha *et al.* [18, 30] to increase the range of applications and improve the physical model. Moreover, some numerical developments have been performed to increase the code efficiency and reduce the numerical errors. The model has been validated on various geometries, such as Venturi type sections, hydrofoils, or blade cascades, and the results showed a good general agreement with experiments. Their specificity is an especially reliable simulation of the cyclic behaviour of unsteady cavitating flows.

Sections 1 and 2 are devoted to the physical approach used in the code and to the main features of the numerical method, particularly the special treatment induced by the two-phase flow model. Validation of the model is performed through unsteady computations of cavitating flows in Venturi type sections, whose experimental behaviour has been studied previously [1, 19, 20]. The sections were designed to simulate the pressure field along the suction side of an inducer blade. Two geometries are considered, namely a 4° and a 8° divergence angle Venturi, the second one leading to a pronounced unsteady behaviour. The details of their geometry are presented in Section 3. The influence of the numerical parameters is studied in the case of the 8° divergent angle, and the results are presented in Section 4. Quantitative comparisons with experimental measurements are analysed in Sections 5 and 6 for both geometries.

2. PHYSICAL MODEL

Generally, two-phase flow models are based on the assumption that the fluid is present in the computational domain both as liquid and as vapour. The vapour is characterized by a density ρ_v, and the liquid by a density ρ_l. On each cell of the mesh, the unknowns are calculated for each phase by averaging them on the volume occupied, respectively, by liquid and gas

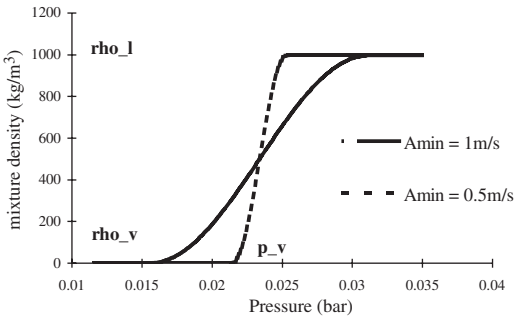

Figure 2. The barotropic state law $\rho(P)$ for water and two different values of the minimum speed of sound $A_{\min}$ in the mixture.

[21]. Neglecting the thermal effects, the number of balance equations in 2D is six because of the two phases. These equations govern the behaviour of the two-phase structures larger than the cells, whereas the smaller structures are modelled by closure laws, which empirically calculate the fluxes of mass and momentum between the two phases. The difficulty of this kind of approach is to evaluate the mass and momentum transfer terms in the balance equations.

In the present work, we apply a single-phase flow model that considers the vapour/liquid mixture as a single fluid [8] characterized by its density ρ. When it equals the liquid one ρ_l, all the cell is occupied by liquid, and if it equals the vapour one ρ_v, the cell is full of vapour. Between these two extreme values, the cell is occupied by a two-phase mixture that is still considered as one single fluid. The void fraction α is defined as the local ratio of vapour contained in this mixture: $\alpha = (\rho - \rho_l)/(\rho_v - \rho_l)$. The fluid density is controlled by a barotropic state law $\rho(P)$ (Figure 2) that links the fluid density variations to the local static pressure evolution: when the pressure is slightly higher or lower than the vapour pressure, the fluid is supposed to be purely liquid or purely vapour, according respectively to the Tait equation [22] and the perfect gas law.

$$\frac{P}{\rho} = \text{Constant} \quad \text{(Perfect gas law for the pure vapour, neglecting thermal effects)}$$

$$\frac{\rho}{\rho_{\text{ref}}} = \sqrt[n]{\frac{P + P_0}{P_{\text{ref}}^{\text{T}} + P_0}} \quad \text{(Tait law for the pure liquid)}$$

where $P_{\text{ref}}^{\text{T}}$ and ρ_{ref} are reference pressure and density.

(Presently, $P_{\text{ref}}^{\text{T}} = P_{\text{outlet}}$, and for water: $\rho_{\text{ref}} = \rho_l$, $P_0 = 3 \times 10^8$ Pa and $n = 7$).

These two quasi-incompressible states are joined smoothly in the vapour pressure neighbourhood, which results in a simple description of the vapourization and condensation processes. The state law presented in Figure 2, close to the one proposed by Jackobsen [23], is characterized mainly by its maximum slope $1/A_{\min}^2$, where $A_{\min}^2 = \partial P/\partial \rho$. The parameter $A_{\min}$ can thus be interpreted as the minimum speed of sound in the mixture. This parameter depends on the two-phase structure of the medium and remains an adjustable parameter of the model.

Concerning the momentum fluxes, our model assumes that locally (in each cell), velocities are the same for liquid and for vapour: in the mixture regions gas structures are supposed to

be perfectly carried along by the main flow. That hypothesis is often used for the problem of sheet-cavity flows where the interface is considered to be in dynamic equilibrium [9, 14]. The momentum transfers between the phases are thus strongly linked to the mass transfers, which are treated implicitly by the state law without any supplementary assumptions.

3. NUMERICAL TREATMENT

The model is developed in two dimensions. We detail here the numerical treatment with a special emphasis on the cavitation process.

3.1. Mesh

We use curvilinear orthogonal co-ordinates and a staggered mesh. The mesh generation is based on the method of Ryskin and Leal [24], optimized for our particular applications [25].

3.2. Governing equations

The physical model presented above leads to one scalar equation for the mass conservation and one vector equation for the momentum conservation. The time-dependent Reynolds averaged Navier–Stokes equations can be written in Cartesian co-ordinates in an absolute stationary frame of reference in the following non-conservative form with the Boussinesq approximation.

$$\begin{aligned}
&\rho\frac{\partial u_x}{\partial t}+\rho u_x\frac{\partial u_x}{\partial x}+\rho u_y\frac{\partial u_x}{\partial y}=-\frac{\partial P}{\partial x}+\mu\left(\frac{\partial^2 u_x}{\partial x^2}+\frac{\partial^2 u_x}{\partial y^2}\right)\\
&\rho\frac{\partial u_y}{\partial t}+\rho u_x\frac{\partial u_y}{\partial x}+\rho u_y\frac{\partial u_y}{\partial y}=-\frac{\partial P}{\partial y}+\mu\left(\frac{\partial^2 u_y}{\partial x^2}+\frac{\partial^2 u_y}{\partial y^2}\right)\\
&\frac{\partial\rho}{\partial t}+\frac{\partial}{\partial x}(\rho u_x)+\frac{\partial}{\partial y}(\rho u_y)=0\\
&\rho=F(P,P_{\text{vap}})
\end{aligned}\tag{1}$$

As we work in the orthogonal frame of curvilinear co-ordinates (ξ,η), we finally obtain by projection in this frame the following equations, written in the general form [26]:

$$\begin{aligned}
&S\frac{\partial}{\partial t}(\rho\Phi)+\nabla_\xi\left(\rho u\Phi-\Gamma_\Phi\frac{\partial\Phi}{\partial\xi}\right)+\nabla_\eta\left(\rho v\Phi-\Gamma_\Phi\frac{\partial\Phi}{\partial\eta}\right)=S_\Phi\\
&\rho=F(Cp,\sigma)
\end{aligned}\tag{2}$$

where Φ stands either for 1, u, or v, Γ_Φ is the diffusion coefficient, u and v are the velocity components along co-ordinates ξ and η, respectively, ∇_ξ and ∇_η are the physical components of the divergence operator along the curvilinear co-ordinates, S_Φ is the source term, Cp is the non-dimensional pressure coefficient, and σ is the cavitation number.

3.3. Spatial discretization

The finite volume method is applied for the space discretization. Each equation is integrated locally on its own control volume based on the staggered grid to avoid pressure oscillations.

The pressure and the density are calculated at the center of the cells, while the velocity components u and v are located, respectively, on the western and the southern faces of each cell.

The divergence term in Equation (2) is first turned into a sum of fluxes through the control volume faces. The diffusive terms are then discretized in a purely central manner, while the convection terms are estimated through the HLPA scheme proposed by Zhu [27]. This is a second-order scheme, which locally switches to first order, to prevent numerical oscillations in critical high pressure gradient areas. This scheme leads to the occurrence of both first-order and second-order terms: it is written like an upwind scheme, completed by a second-order term taken at the previous iteration. This last term is thus explicit, and it is added to the right hand side of the algebraic system.

Although the simulation is two-dimensional (only two components u and v of the velocities are considered), the cells are three dimensional. Their width evolution throughout the computational domain allows one to simulate the influence of radius in axisymmetric cases or to take into account smooth variations of the stream sheet width.

3.4. Temporal discretization

Several numerical schemes of first and second order are available. An unconditionally stable, first-order implicit scheme is usually applied, which corresponds to the following expression for the time-dependent terms:

$$\frac{\partial(\rho\Phi)}{\partial t} = \frac{\rho^{n+1}\Phi^{n+1} - \rho^n\Phi^n}{\Delta t} \tag{3}$$

Time-step and scheme order influence have been investigated (see Section 4) to check that the numerical errors induced by this discretization are acceptable. A second-order integration scheme was thus also applied:

$$\frac{\partial(\rho\Phi)}{\partial t} = \frac{1.5\rho^{n+1}\Phi^{n+1} - 2\rho^n\Phi^n + 0.5\rho^{n-1}\Phi^{n-1}}{\Delta t} \tag{4}$$

3.5. Turbulence model

A standard k–ε RNG turbulent closure model [28], adapted for two-phase flow simulations, is used. The standard turbulence model considers a viscosity $\mu = \mu_t + \mu_l$

$$\begin{aligned} &\text{where} \quad \mu_l \text{ is the laminar viscosity} \\ &\qquad \mu_t = f(\rho)C_\mu k^2/\varepsilon \text{ is the turbulent viscosity} \\ &\qquad C_\mu = 0.085 \end{aligned} \tag{5}$$

The standard function $f(\rho) = \rho$ is for the general case of a single-phase fluid. An arbitrary diminution of the turbulent viscosity in the two-phase regions was proposed to improve the modelling of the unsteady self-oscillatory behaviour of sheet cavitation [1]. Therefore, we introduced a modified function f (Figure 3) of the form:

$$f(\rho) = \rho_v + \alpha^n(\rho_l - \rho_v) \quad \text{with } n > 1 \tag{6}$$

The function f is then equal to ρ_v or ρ_l in the regions containing, respectively, pure vapour or pure liquid, but it decreases rapidly toward ρ_v for intermediate void ratios. Coutier-Delgosha

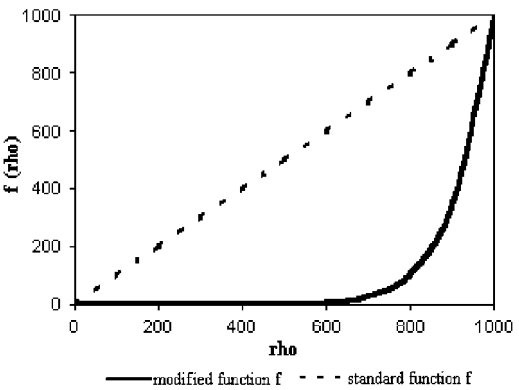

Figure 3. Modification of the turbulent viscosity.

et al. (2001) have shown that this arbitrary modification of the model amounts to taking into account effects of the vapour/liquid mixture compressibility on the turbulence structure.

3.6. Computational procedure

The numerical resolution must be adapted to both compressible fluids (to treat the vapourization and condensation processes) and quasi-incompressible fluids (in pure liquid and pure vapour areas). In compressible simulations, the pressure is usually linked to the velocity **U** and the density ρ through the state equation. In incompressible simulations, this is not the case anymore, since the equation of state becomes almost $\rho = \text{constant}$. Thus, we use a classical pressure-correction method proposed by Patankar [16]. It is based on the SIMPLE algorithm, modified to include the k–ε resolution and the cavitation treatment. Only the main features are presented here, details can be found in Reference [25].

The algorithm is an iterative process. The resolution of each time-step is divided into several iterations, which march the solution towards convergence. Each iteration is composed of two successive steps. The velocities are first estimated by a resolution of the momentum equations without any modification of the pressure. Then, these values of u and v are corrected through the resolution of a 'pressure correction' equation, in order to satisfy the continuity. The cavitation process induces the following modifications:

- The density ρ is first calculated with the barotropic state law after the momentum equations resolution, as well as its derivative $\partial\rho/\partial P$.
- When the pressure correction $\mathrm{d}P$ is obtained, the density values are corrected:

$$\mathrm{d}\rho = \left(\frac{\partial \rho}{\partial P}\right)\mathrm{d}P \tag{7}$$

A supplementary loop over the pressure correction step is then added inside each iteration to check that the void ratio remains inside its physical range $[0, 1]$.

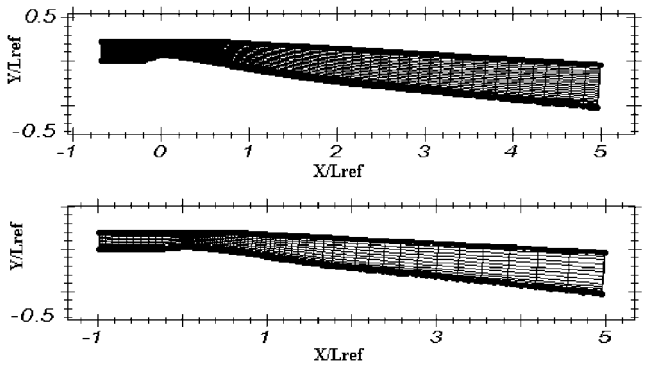

Figure 4. The coarse meshes of the two cases: (a) 8° angle and (b) 4° angle.

3.7. Boundary conditions

The boundary conditions are based on a system of dummy cells. Two rows of supplementary cells are generated around the computational domain. By imposing the values of variables in these cells, all standard boundary conditions are available: velocity, pressure, wall condition, connections (matching or non-matching), periodicity. The non-matching connections are treated with an interpolation method especially adapted to our algorithm, and the details can be found in Reference [18]. A multidomain procedure was also developed, for blade cascades applications.

Classical incompressible type of boundary conditions are applied: imposed velocities at the inlet, and an imposed static pressure at the outlet. Numerical studies have been performed to improve these conditions, mainly by taking into account the test rig influence [33]. They were not applied in the present application.

3.8. Unsteady treatment

In experiments, the classical cavitation test consists of setting initially a relatively high pressure in the flow field, for which no vapour appears. Then, the static pressure is decreased until the desired cavitation number σ is reached.

We developed a similar numerical procedure: first of all, a stationary step is carried out with an outlet pressure high enough to avoid any vapour in the whole computational domain. Then, this pressure is lowered smoothly at each new time-step down to the value corresponding to the desired cavitation number. Vapour appears as the pressure decreases. The cavitation number is then kept constant throughout the computation.

4. GEOMETRIES

Numerical simulations have been performed on two Venturi type sections whose divergent angle is 8° and 4°, respectively (Figure 4). In both cases, cavitation occurs at the Venturi throat. The shape of the Venturi bottom downstream from the throat simulates the suction side of an inducer blade with a beveled leading edge geometry [34] and a chord length L_{ref}.

These geometries were tested previously by Stutz and Reboud [19, 20] and the experimental data are used in the present work to validate the numerical simulations.

According to experimental observations:

- The first geometry, with large convergent–divergent angles (18–8°) leads to a cyclic unsteady cavitation showing quasi-periodic fluctuations. Each cycle is composed of the following successive steps: the cavity grows, and a re-entrant jet composed of a liquid/vapour mixture flows upstream along the Venturi bottom until the cavity breaks off. The cloud of vapour is then convected by the main stream, and it finally collapses [19].
- The second geometry is characterized by small convergent–divergent angles (4.3°–4°) and a smaller contraction ratio at the throat. In this case stable cavities are observed, with only small-scale fluctuations in their downstream part [20].

These two behaviours are very different, so the two Venturi type sections are adequate test cases: the objective is to simulate efficiently the two configurations, with the same physical and numerical model.

5. VALIDATION TESTS

Validation tests were performed with the 8° divergent cavitation tunnel whose behaviour is fundamentally unstable. Our reference simulation corresponds to an inlet velocity $U_{\text{ref}} = 7.2\,\text{m/s}$ and a cavitation number $\sigma = 2.4$. These conditions lead experimentally to self oscillating cavitation with a visual length of the attached sheet cavity $L_{\text{cav}} = 50\,\text{mm}$ and a cloud shedding frequency of 45 Hz. Twenty T_{ref} of simulation are performed, where T_{ref} is a reference time corresponding to the time necessary for the flow field to cover the length $L_{\text{ref}} = 0.23\,\text{m}$ with the speed U_{ref}.

5.1. Turbulence model discussion

The unstable cavitating behaviour is not correctly simulated if we use a standard k–ε RNG turbulence model. In this case after a transient fluctuation of the cavity length, we obtain a quasi-steady behaviour of the cavitating flow and a complete stabilization of the cavitation sheet (Plate 1). The resulting cavity length is too short compared to the experimental observations. Even when taking into account the liquid separated flow downstream of the vapour sheet as part of the cavity, the total length remains about 2 times smaller than the value reported from the experiment. This result is not significantly modified if the mesh size or the time step are changed.

To obtain a cavity length closer to the experimental one, the imposed cavitation number must be reduced to about $\sigma = 2.0$. In that case, local comparisons are investigated with experimental data obtained by double optical probes measurements. This technique and the results are presented in detail in References [19, 20]. This is an intrusive captor, which allows measurements of the local void ratio and the velocities of the two-phase structures inside the cavitation sheet. Four data profiles, whose position is indicated on Figure 5, are available.

The time-averaged and standard deviation values of void ratio α and velocity u are presented for each profile on Figure 6. The dotted line corresponds to the experimental external shape of

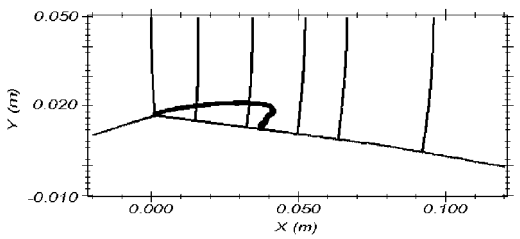

Figure 5. Data profiles and cavity contour (σ adjusted to obtain a cavity length close to experimental observations).

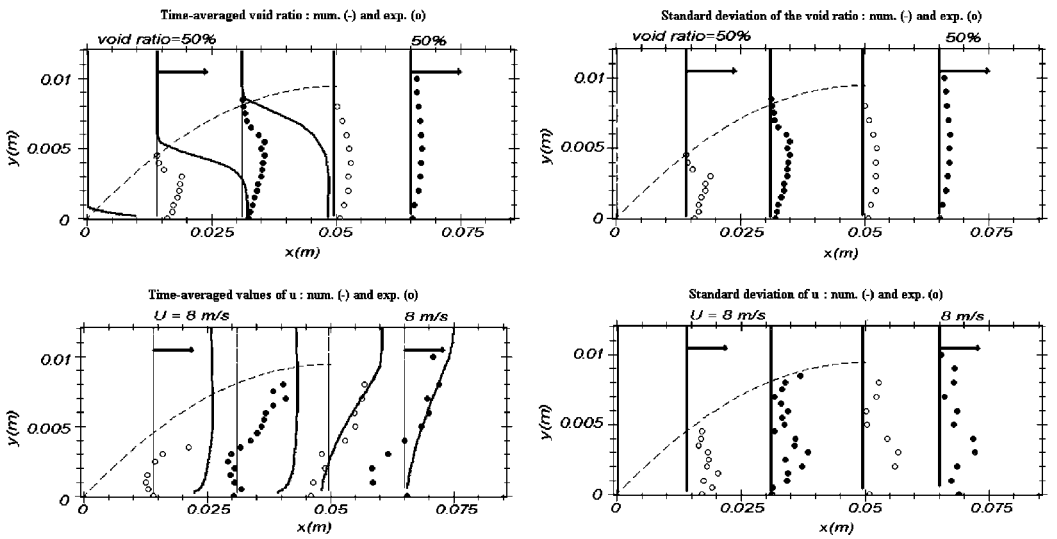

Figure 6. Time-averaged and standard deviation values of void ratio α and velocity u Comparison between numerical results (lines) and optical probes measurements (points). $U_{\text{ref}} = 7.2$ m/s, $\sigma_{\text{exp}} = 2.4$—Standard k–ε model. ($\sigma_{\text{num}} = 2.0$, adjusted to obtain a cavity length corresponding to experimental observations) (cavity external shape in dotted line from image processing). Ratio 3 between vertical and horizontal scales.

the cavity, deduced from visualizations. It shows the poor agreement between the numerical and experimental results:

- The numerical mean void ratio is over-estimated in the upstream part of the cavity. Calculations give a high void ratio (larger than 90%), abruptly falling to 0% in the wake, while the measured void ratio never exceeds 25% and decreases slowly from the cavity upstream end to its wake. The time-averaged velocities are also incorrect in the cavitation sheet, since the re-entrant jet is not well predicted. On the other hand, the mean velocity profiles downstream of the cavity are in quite good qualitative agreement with measurements.

- The most important discrepancy with the experimental measurements concerns the fluctuations: experimental standard deviation values are of the same order of magnitude as the mean values; whereas, the numerical ones are zero, since the cavity is stabilized.

This poor agreement with the real configuration seems to be related to an over-prediction of the turbulent viscosity in the rear part of the cavity. As a matter of fact, the transient analysis of the cavity behaviour obtained by non-viscous fluid calculations indicated that the main problem in the turbulent flow simulations consisted in the premature removal of the reverse flow along the solid wall: the re-entrant-jet was stopped too early and it did not result in any cavity break off.

This major discrepancy is probably partially linked to the classical limitations of the k–ε turbulence model in the case of separated flows [29]. Moreover, the standard k–ε RNG model does not take into account the compressibility effects on turbulence, since it is devoted to fully incompressible flows. According to the adopted barotropic state law, in the mixture vapour/liquid zones the sound celerity is very low, and the fluid is highly compressible (the Mach number can be larger than 5). Several turbulence models have been tested by Coutier-Delgosha *et al.* [30] in this configuration, and the reduction of the effective viscosity obtained in the compressible areas with a k–ω model including compressibility effects [29] seems to be of primary importance to simulate the cyclic cavitation behaviour.

5.2. *Validation of the global cavitating behaviour with the modified k–ε model*

We performed a first attempt to improve the simulation, simply by arbitrarily reducing the turbulent viscosity in the low void ratio areas. This modification, that was detailed in Section 2, is applied with the parameter $n = 10$, leading to a very quick decrease of the turbulent viscosity as soon as the density decreases below the pure liquid one. It leads to substantial changes in the simulation. The unsteady re-entrant jet seems now correctly predicted, and we obtain vapour cloud shedding. Plate 2 presents the typical shape of the biggest attached cavity obtained in this reference case.

The transient evolution observed during this unsteady calculation is presented in Plate 3. Plate 3(a) illustrates at a given time and for each cross section of the Venturi type duct the value of the minimal density present in the section. By comparison with Plate 1, it gives information concerning the vapour cloud shedding process: the part of the cavity that breaks off clearly appears, and the fluctuation frequency can be easily calculated. Moreover, it also supplies the maximum void ratio in each section. The two other curves (Plate 3(b) and (c)) represent, respectively, the total vapour volume and the inlet pressure evolutions.

The experimental self-oscillatory behaviour of the cavitation sheet is correctly simulated with a fluctuating attached cavity whose maximum length is about 45 mm (i.e. $L_{cav}/L_{ref} = 0.2$, cf. Plate 3). Its mean fluctuation frequency is estimated by FFT transform of the inlet pressure signal after the initial transient. It equals $52\,\text{Hz} \pm 3\,\text{Hz}$. The length is now almost correctly predicted, only 10% smaller than the mean experimental value of 50 mm, while the oscillation frequency is about 15% larger than the experimental one. Because the frequency of the self-oscillation behaviour decreases when the cavity length increases, these two results might be both improved by a small decrease in the imposed cavitation number.

The transient evolution is almost periodic. This behaviour is consistent with the experimental observations, which mention a quite regular cavitation cycle whose frequency oscillates around a central value [19, 20]. Although the present result (Plate 3) is quite regular, we

Table I. Tested parameters.

Parameter	Range	Reference value
Numerical parameters		
Mesh dimensions (three sizes were tested)	$110*30$–$160*50$–$264*90$	160*50
Non-dimensional time step DT/T_{ref}	$0.002 \rightarrow 0.01$	0.005
Time discretization scheme TO	1st order–2nd order	1st order
Physical parameters		
Maximum slope of the barotropic law A_{min} (m/s)	$1\ m/s \rightarrow 4\ m/s$	1.44
Ratio ρ_v/ρ_l	$0.001 \rightarrow 0.1$	0.01
Cavitation number σ	2.32 (blockage)$\rightarrow$ 2.52 (small cavity)	2.41
Parameter n of the turbulence model	$5 \rightarrow 20$	10

sometimes observe some random disturbances affecting the oscillation cyclic behaviour. Our whole computations suggest that, after the initial growing of the cavity is finished, only a couple of regular cycles can be obtained between two perturbations. These perturbations are usually caused by a late implosion of the vapour cloud, which delays the growing of the next cavity.

The influence of the number n value was investigated and results are given in the next section. This parameter was found to have almost no influence on the self-oscillatory behaviour of the sheet of cavitation, so far this behaviour is obtained, i.e. for values of n high enough to give a quick decrease of the turbulent viscosity in the liquid–vapour mixture regions. The value of $n = 10$ was chosen for all the computations presented in the present paper.

5.3. Numerical tests

Influence of numerical and physical parameters on the convergence rate and on the result is tested in this section with the previous geometry. As the final cavity obtained is fundamentally unstable, it cannot be characterized by its final shape or the final void ratio. The comparisons are thus based on the transient evolution of the cavitating flow. This evolution can be defined at each time by the vapour quantity present in the domain or by the cavity shape (length, volume). Since all these parameters have the same type of time evolution, we focus on the vapour volume oscillations. For each computation, we calculate the time-averaged vapour volume and its standard deviation. We also estimate the cavitation cycle frequency according to the inlet pressure signal analysis. Results are considered after $T/T_{ref} = 5$ to eliminate the initial transient. Table I presents the parameters that were investigated, with their corresponding range, and the reference value applied for the simulations in the next sections. The results of the tests are presented in Table II.

Concerning the numerical parameters: The mesh obviously has a strong influence on the result of the simulation: the finer it is, the more the time-averaged vapour volume increases. The standard deviation also strongly depends on the mesh size in the cavity area. Nevertheless, its influence on the cloud shedding frequency is very weak, so far the mesh is fine enough: for a time-step $DT = 0.005\,T_{ref}$, we obtain 20% deviation between the coarsest mesh ($110*30$) and the reference one ($160*50$), but this difference falls down to 2% between this mesh and the finest one ($264*90$). The frequencies obtained with a smaller time-step (0.002) are also

Table II. Results of the tests of the physical and numerical parameters in the case of the 8° Venturi type section.

							Results		
σ	A_{min} (m/s)	ρ_v/ρ_l	DT	Mesh	TO	n	Mean vapour volume ($\times 10^{-4}$ m^3)	Oscillation frequency (Hz)	Standard deviation ($\times 10^{-4}$ m^3)
				Reference case					
2.4	2	0.01	0.005	160 * 50	1	10	11.0	55	2.4
				Influence of the time step					
2.4	2	0.01	0.002	160 * 50	1	10	12.3	51	4.3
2.4	2	0.01	0.005	160 * 50	1	10	11.0	55	2.4
2.4	2	0.01	0.01	160 * 50	1	10	9.3	55	2.7
				Influence of the mesh					
2.4	2	0.01	0.002	264 * 90	1	10	15.6	52	2.9
2.4	2	0.01	0.005	264 * 90	1	10	14.5	54	4.3
2.4	2	0.01	0.005	160 * 50	1	10	11.0	55	2.4
2.4	2	0.01	0.005	110 * 30	1	10	6.9	64	1.9
				Influence of the time order					
2.4	2	0.01	0.005	160 * 50	1	10	11.0	55	2.4
2.4	2	0.01	0.01	160 * 50	2	10	12.1	51	4.8
2.4	2	0.01	0.002	160 * 50	2	10	13.4	51	4.5
2.4	2	0.01	0.002	264 * 90	2	10	15.1	52	3.7
				Influence of the cavitation number					
2.32	2	0.01	0.005	160 * 50	1	10	123	17	32.9
2.34	2	0.01	0.005	160 * 50	1	10	44.3	30	9.1
2.37	2	0.01	0.005	160 * 50	1	10	19.7	41	5.8
2.4	2	0.01	0.005	160 * 50	1	10	11.0	55	2.4
2.44	2	0.01	0.005	160 * 50	1	10	6.9	68	1.9
2.52	2	0.01	0.005	160 * 50	1	10	4.4	82	1.6
				Influence of Amin					
2.4	1	0.01	0.005	160 * 50	1	10	9.7	54	3.6
2.4	2	0.01	0.005	160 * 50	1	10	11.0	55	2.4
2.4	3	0.01	0.005	160 * 50	1	10	14.1	51	1.6
2.4	4	0.01	0.005	160 * 50	1	10	14.8	43	1.9
				Influence of the parameter n					
2.4	2	0.01	0.005	160 * 50	1	7	11.4	55	2.2
2.4	2	0.01	0.005	160 * 50	1	10	11.0	55	2.4
2.4	2	0.01	0.005	160 * 50	1	20	11.1	54	2.9
				Influence of the ratio ρ_v/ρ_l					
2.4	2	0.001	0.005	160 * 50	1	10	10.6	57	2.4
2.4	2	0.01	0.005	160 * 50	1	10	11.0	55	2.4
2.4	2	0.1	0.005	160 * 50	1	10	9.5	55	2.9

very close in the case of the two finest meshes (4% deviation). We thus consider that the unsteady cavitating flow pattern is correctly simulated with the two finest meshes.

The time-step influence appears to be strong so far it is not small enough: the differences between the biggest one (0.01) and the reference one (0.005) are noticeable. A part of these

discrepancies is surely due to the random disturbances that highly affect some of the computations, and prevent us from performing clear and precise comparisons (these disturbances are fully consistent with the experimental observations). The two smallest values (0.005 and 0.002) lead to closer results concerning the mean vapour volume (less than 10% deviation in the case of the finest meshes). The cavitation cycle frequency still oscillates around 50/55 Hz, which suggests that the influence of the time step cannot be completely removed.

This numerical influence of the time step on the results led us to investigate second-order time-accurate simulations. Time step 0.01 was tested with the standard mesh, and then time step 0.002 was tested with the standard and the finest mesh. Although the mean vapour volume and the standard deviation do not seem to become constant, they clearly remain of the same order of magnitude. The oscillation frequency stabilizes around 51/52 Hz, which is very close to the result obtained with the first-order scheme (oscillation frequency between 51 and 55 Hz). It confirms that dissipation induced by the first-order time integration scheme has only a little influence on the vapour cloud shedding simulation. So this configuration will be applied hereafter with the time-step 0.005. The phenomenon frequency will be systematically slightly over-estimated, but it must be considered that the random variations of the experimental behaviour are of the same order of magnitude.

Concerning the physical parameters: An increase of $A_{\min}$ leads to a decrease of the slope of the barotropic law. It induces a smoothing of the pressure gradients, and thus an increase of the cavity thickness. The resulting vapour volume also increases. On the contrary, the standard deviation is reduced, which can be related to the gradients smoothing: the dissipation in the rear part of the cavity increases, and the cavitation sheet is stabilized. The reference value of $A_{\min}(0.3 * U_{\text{ref}} \approx 2\ \text{m/s})$ is chosen so that the thickness of the cavity is consistent with experimental results, for several different cavity lengths. This choice will be used in the quantitative comparisons in the next paragraph.

The influence of the density ratio ρ_v/ρ_l appears very small: the vapour volume difference between the case $\rho_v/\rho_l = 0.001$ and the case $\rho_v/\rho_l = 0.01$ is less than 4%. The difference is more noticeable (14%) between the case $\rho_v/\rho_l = 0.01$ and the case $\rho_v/\rho_l = 0.1$. It suggests that the influence of this parameter becomes negligible when it decreases below 0.01. So the reference value 0.01 is chosen.

A large range of the cavitation number was investigated, and the code showed its ability to simulate critical cavitating behaviours: even in the case $\sigma = 2.32$, which almost corresponds to the blockage of the Venturi section, the computation goes on satisfactorily.

These tests validate the reference values for all the numerical parameters used here after.

6. RESULTS IN THE 8° VENTURI TYPE SECTION

Computations have been carried out considering the 8° Venturi section, which presents an unstable cavitation behaviour involving large cloud shedding. The configuration is the one presented in Section 4 and all the parameters are set to their reference value. We use the modified k–ε turbulence model. Comparisons are first made with measured frequencies (Figure 7) and experimental visualizations of the cavity shape (Plate 4), and a local validation of the results is performed by comparison with experimental data obtained by optical probes measurements within the cavitation sheet (Figure 8).

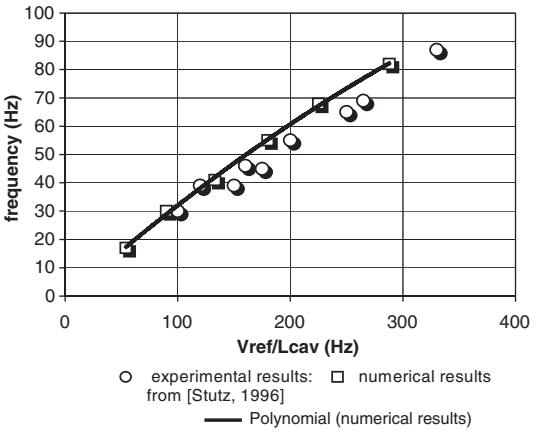

Figure 7. Experimental and numerical oscillation frequency.

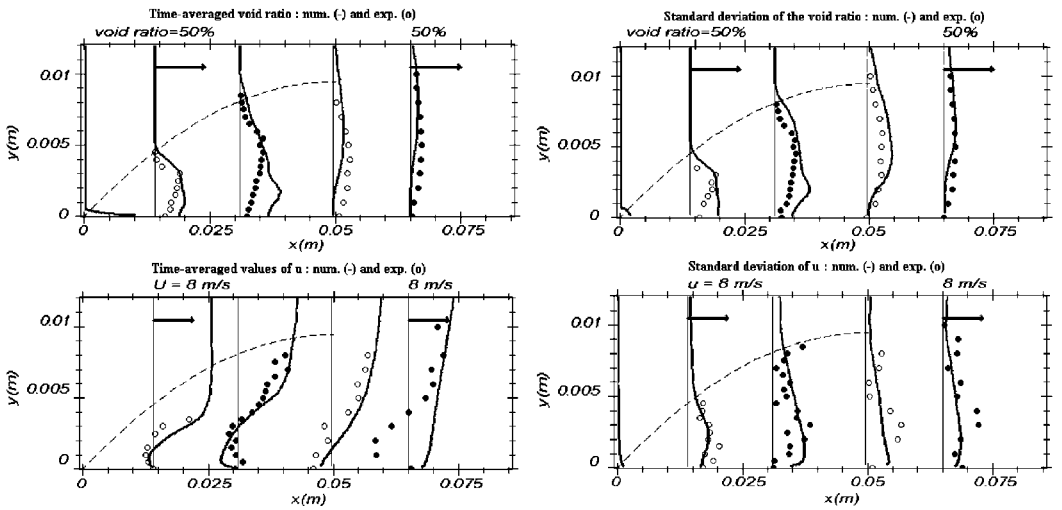

Figure 8. Time-averaged and standard deviation values of void ratio α and velocity u. Comparison between numerical results (lines) and optical probes. Measurements (points)—$U_{\text{ref}} = 7.2\,\text{m/s}$—modified k–ε model, $(L_{\text{cav}})_{\text{mean}} = 50\,\text{mm}$ (cavity external shape in dotted line from image processing)—ratio 3 between vertical and horizontal scales.

6.1. Shedding frequency

From the results of Table II concerning the effect of the cavitation number, a comparison can be proposed with results reported by Stutz [35]: the frequency of the self-oscillation behaviour is drawn with respect to the ratio $V_{\text{ref}}/L_{\text{cav}}$. The maximum length of the attached cavity given by the numerical simulation is chosen as an estimation of the visual length reported from the experiments. That length varies as the square root of the total time-averaged vapour volume. It can be seen in Figure 7, that a good agreement can be found for a large range of cavitation

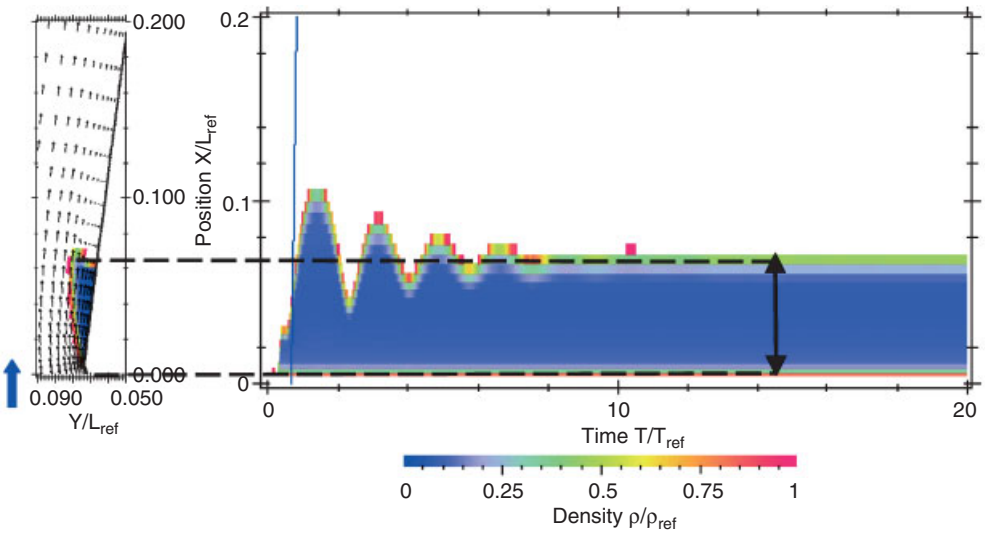

Plate 1. Time evolution of the cavity length with a standard k–ε turbulence model. The time is reported in abscissa, and the X position in the tunnel of cavitation is graduated in ordinate. The colours represent the density values: white for the pure liquid one and from red to dark blue for the vapour one. At a given point in time and position, the colour indicates the minimum density in the corresponding cross section of the cavitation tunnel. *Calculation conditions*: $\sigma_{\text{num}} = 2.4$; $U_{\text{ref}} = 7.2\,\text{m/s}$; *mesh size* $= 160 \times 50$; *time step* $\Delta t = 0.005 T_{\text{ref}} (T_{\text{ref}} = L_{\text{ref}}/U_{\text{ref}})$.

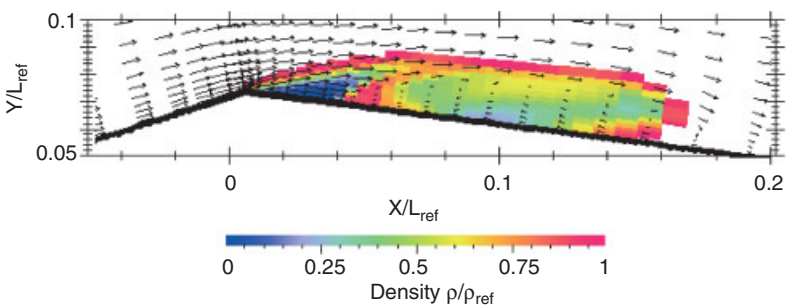

Plate 2. Shape of the attached sheet cavity just before its break-off. $\sigma_{\text{num}} = 2.4$, $160 * 50$ mesh, velocity vectors drawn only 1 cell over 2 in the two directions.

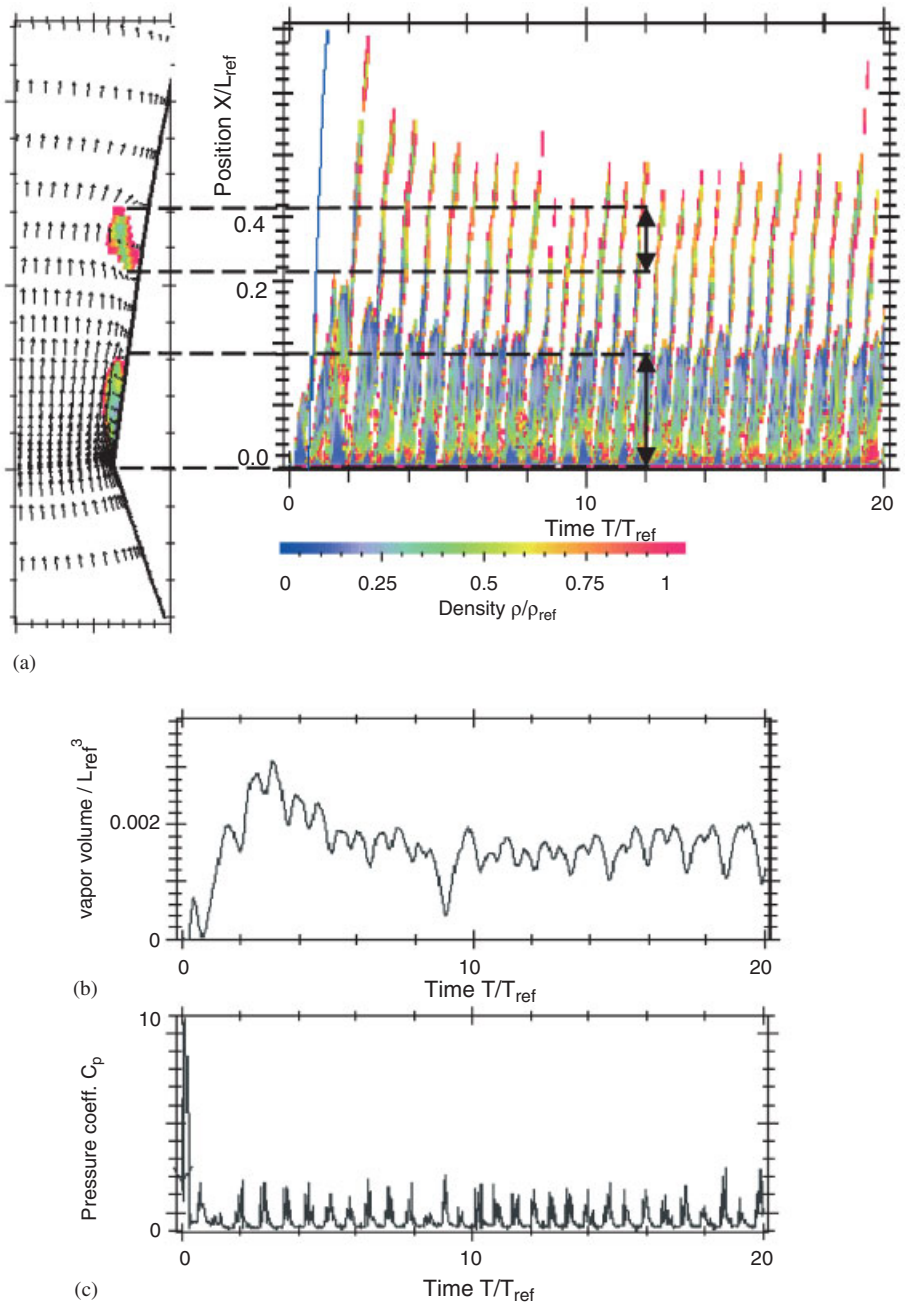

Plate 3. Transient evolution of unsteady cavitating flow in the 8° Venturi type duct. (a) Temporal evolution (in abscissa) of the cavity length (graduated in ordinate) (Instantaneous attached and cloud cavities at $T = 12T_{\text{ref}}$ are given at left). (b) Time evolution of the volume of vapour in the flow field. (c) Time evolution of the inlet pressure: $(P_{\text{inlet}} - P_{\text{outlet}})/1/2\rho_{\text{l}}U_{\text{ref}}^2$.

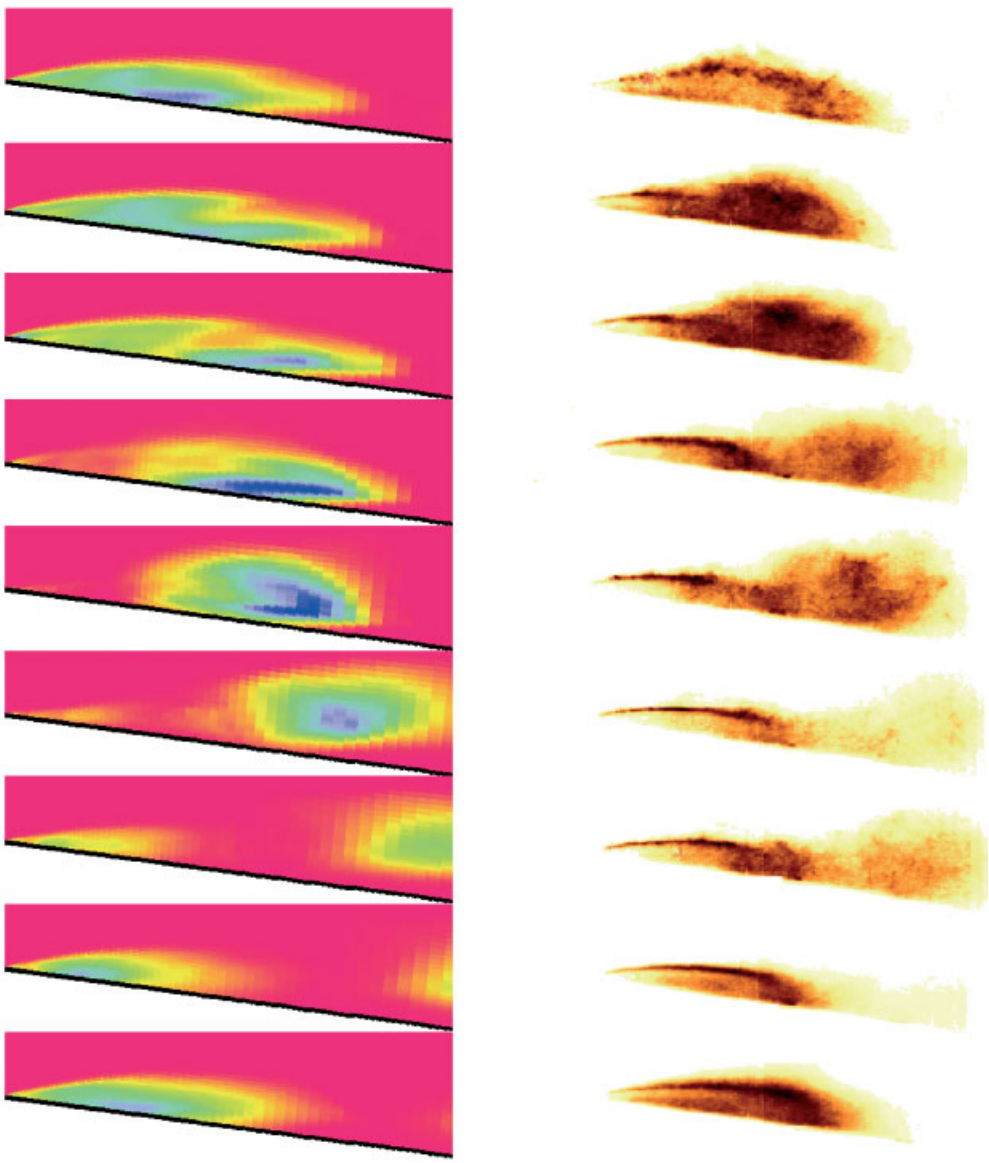

Plate 4. Numerical and experimental phase-averaged sequences of unsteady cavitation behaviour in the 8° divergent cavitation tunnel mean attached cavity length $L_{cav} = 50$ mm, $U_{ref} = 7.2$.

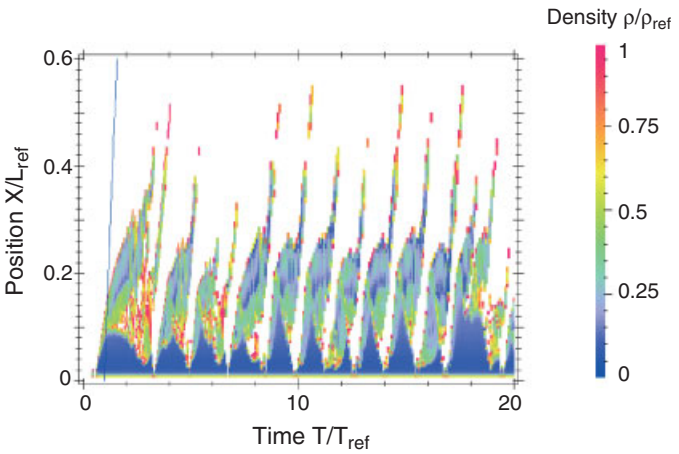

Plate 5. Evolution of the cavity length with the modified k–ε model.

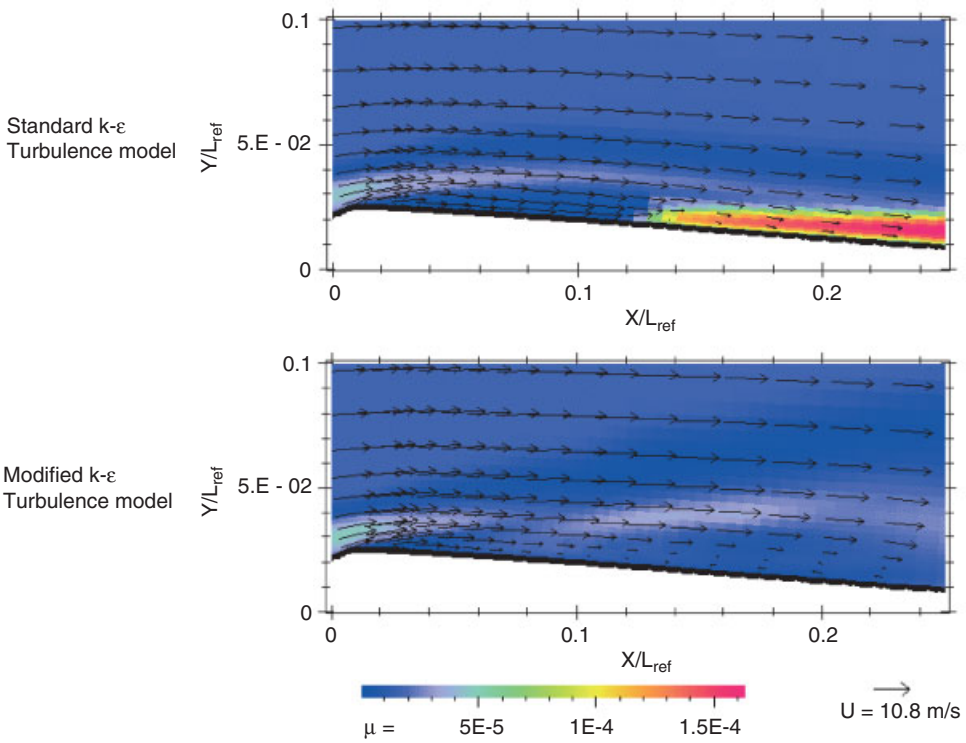

Plate 6. Comparisons between the two turbulence models.

number and corresponding cavity length. Dividing the shedding frequency by the ratio $V_{\text{ref}}/L_{\text{cav}}$ gives an almost constant Strouhal number 0.27 ± 0.02.

6.2. Description of the cavitation cycle

Two phase-averaged cavitation cycles are presented in Plate 4. The right one results from experimental visualizations: Video frames acquired during a 100 ns exposure time under Laser sheet light are identified and digitized in 256 grey levels. A sampling technique is applied to classify them in nine sets corresponding to the different states of the recorded quasi-periodic pressure signal. Then, averaging the grey levels pixel per pixel for each set allows drawing a sequence of phase-averaged images, from an initial data set of 300 frames. Maximum standard deviation computed for each set is about 2/3 of the maximum mean grey level, and it is mainly observed along the attached cavity and cloud boundaries.

The left part of the Plate 4 corresponds to the same sequence obtained by numerical simulation. This one lasts 20 T_{ref}, i.e. about 30 cycles. The same sampling technique is applied: the computational result is decomposed into 30×9 short sequences corresponding to the nine steps of the cavitation cycle and the phase-averaging process is applied. We observe a good agreement between the two results concerning the external shape and global structure of both attached cavity and vapour cloud shed.

6.3. Local comparison with optical probes measurements

The velocity u and the void ratio α are compared along four profiles whose position was indicated on Figure 5. The time-averaged and standard deviation values are represented in Figure 8.

The mean void ratio in the upstream part of the cavity is quite small: only 25%, instead of 90% for the results obtained previously with the standard k–ε model (Figure 6). Fluctuations are very strong with a standard deviation value often larger than the time-averaged value.

The experimental velocity profiles are rather irregular because of the great unsteadiness of the cavitation sheet. Nevertheless good agreement can be noticed between experimental and numerical profiles of both time-averaged and fluctuation values of void ratio and velocity. The presence of the periodic re-entrant jet is noticeable on these velocity profiles whose mean values are close to zero on about one-half of the cavity thickness above the wall.

Our simple modification of the turbulence model had the expected effect: the viscosity decreased in the reverse flow area, and the re-entrant jet was strong enough to break-off a part of the cavity. It leads to a much more realistic behaviour and internal structure of the cavitation sheet.

7. RESULTS IN THE 4° VENTURI TYPE SECTION

Computations were performed with the 4° divergent cavitation tunnel. The experimental visualizations show in this case a quite stable cavity, with fluctuations mainly affecting the downstream part, and only little vapour cloud shedding [20]. This behaviour is thus very different from the previous one, which makes this geometry an interesting complementary test case for the numerical model, applied with exactly the same parameters. The inlet velocity equals 10.8 m/s. Twenty T_{ref} of simulation are performed with a standard 150×50

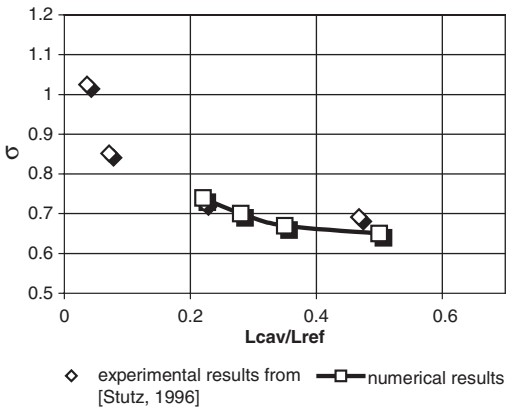

Figure 9. Numerical and experimental results $L_{cav}(\sigma)$.

mesh. The numerical parameters are set to their reference values, and A_{min} still equals 2 m/s (i.e. $0.2 \times U_{ref}$). We use for the simulations the modified k–ε model. The reverse flow near the wall is correctly predicted, and thus we obtain vapour cloud shedding. They are not as large as in the 8° Venturi case, because the cavity thickness is smaller than in the previous configuration, and the cavity breaks off at about its mean length. Only the downstream half of the cavity is then convected and collapsed by the main liquid flow (cf. Plate 5).

Several simulations were performed to check the accuracy of the model for a large range of cavitation numbers. Each result is then averaged in time, to obtain the mean cavity length L_{cav}. The resulting numerical law $L(\sigma)$ is compared to an experimental one (see (Stutz, 1996)) in the Figure 9. We obtain a very good agreement of the mean cavity lengths, which confirms the ability of the model to provide an accurate prediction of the global cavitating behaviour. Calculations corresponding to short cavities are not reported here: stable cavities are obtained as with the standard k–ε turbulence model, their length being then much too small. It suggests that the modification proposed in the turbulence modelling is not completely efficient with this Venturi type section, in which the cavitation behaviour is neither completely stable, nor regularly unstable.

Local comparisons with experimental results inside the cavity are presented hereafter. The experimental data are obtained by double optical probes measurements (see Section 5). The simulation corresponds to a cavitation number $\sigma = 0.7$. The data profiles position is presented in Figure 10.

Comparisons between numerical profiles and experimental ones are presented in Figure 11. The cavity shape is in good agreement with the experimental one. The void ratio in the upstream part of the cavity is much larger than in the previous configuration: 80% for the first profile, instead of 25% in the other Venturi case. The mean values are particularly close to experimental data, and the standard deviation values are also correctly predicted, even if they are a little over-estimated above the cavity. The velocity profiles are also satisfactory. Despite the rather stable behaviour observed during experiments, a mean reverse flow can be noticed along the whole cavitation sheet. It results in a complex two-phase structure inside the cavity, detailed in Reference [20]. The good general agreement obtained has to be associated with the unsteady behaviour predicted by the numerical model.

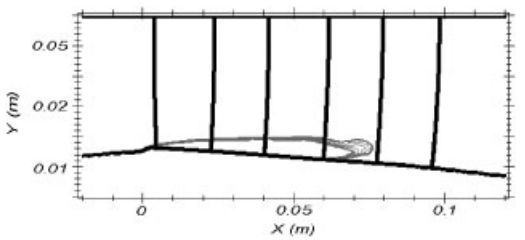

Figure 10. Data profiles position and mean external shape of the cavity (modified k–ε RNG turbulence model).

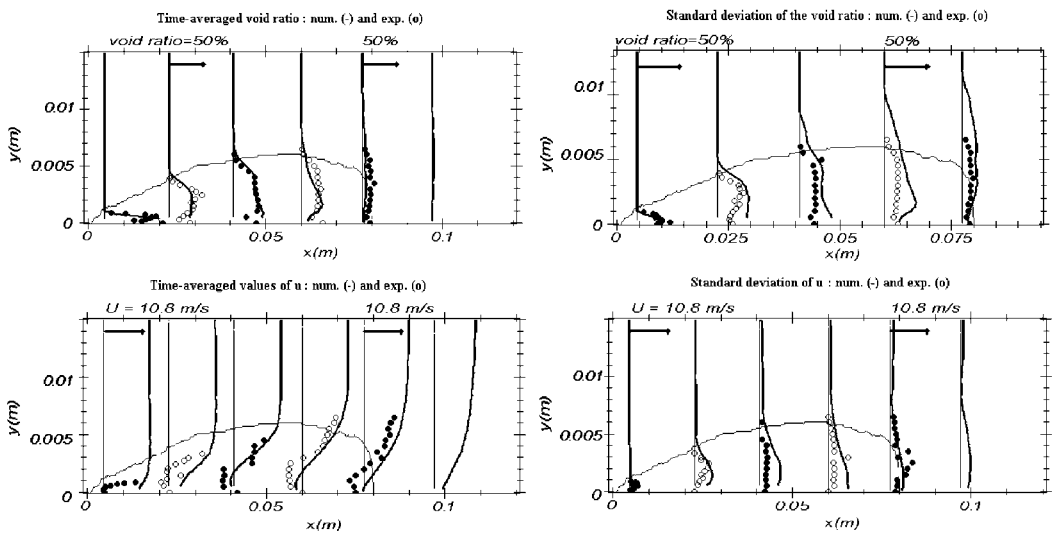

Figure 11. Time-averaged and standard deviation values of void ratio α and velocity u. Comparison between numerical results (lines) and optical probes measurements (points). $U_{\text{ref}} = 10.8$ m/s—modified k–ε model, $(L_{\text{cav}})_{\text{mean}} = 80$ mm (cavity external shape in dotted line from image processing). Ratio 3 between vertical and horizontal scales).

The differences between the two turbulence models (standard or modified k–ε model) are illustrated by Plate 6, which shows the time-averaged turbulent viscosity field and the reverse flow near the Venturi bottom in the two cases. Actually, we observe after the modification a great decrease of the viscosity in the downstream part of the cavity, associated with the appearance of a reverse flow near the wall. It confirms that the over-prediction of the viscosity in the standard turbulence model case is responsible for the complete stabilization of the cavity. A more detailed study is necessary to further investigate the physical mechanisms that affect the turbulence in highly compressible media and during the vapourization/condensation phenomena.

8. CONCLUSION

A 2D model for unsteady cavitation was presented in this paper. Simulations were performed on two Venturi type sections, characterized by divergence angles of 4 and 8°.

The unsteady behaviour of the cavitating flow depends strongly on the turbulence model, and it has a great effect on the mean and fluctuating fields of void ratio and velocity in the cavity. The standard k–ε RNG model leads in the two geometries to quasi-steady cavitation sheets, whose length is under-estimated with respect to visual observations, velocity and void ratio fields within the cavity showing a poor agreement with experimental measurements.

A simple modification of the turbulence model was proposed to reduce the effective viscosity in the mixture. Further investigations presented in Reference [30] have showed that this modification consists of taking into account the influence of the liquid/vapour mixture high compressibility on the turbulence structure. Nevertheless, the present reduction of viscosity in the two-phase areas remains interesting in itself, because it allows very simple modifications of existing numerical codes, without the implementation of a new turbulence model.

Good agreement with measurements was then obtained: the self-oscillation behaviour of cavitation observed in the case of the Venturi with a 8° divergence angle is correctly simulated, with a good estimation of the vapour cloud shedding frequency. Influence of the model and computation parameters has been widely studied. In the Venturi with a 4° divergence angle, an unsteady behaviour is also obtained, with smaller amplitude of the cloud shedding phenomenon. In the two geometries, averaged and RMS values of void ratio and velocities inside the cavity are then consistent with the experimental data. Thus, the proposed model was found to simulate efficiently as well pronounced unsteady behaviours with large vapour cloud shedding (Venturi 8°) as more stable configurations with fluctuations affecting only the rear part of the cavity (Venturi 4°).

NOMENCLATURE

$A_{\min}$	minimum speed of sound in the mixture (m/s)
C_p	$(P - P_{ref})/1/2\rho_l U_{ref}^2$ pressure coefficient (dimensionless)
L_{ref}	'Chord' length of the Venturi profile (m)
P	local static pressure (Pa)
P_{ref}	reference pressure = inlet mean static pressure (Pa)
P_{tot}	total pressure = $P + 1/2\rho_l U_{ref}^2$ (Pa)
P_{vap}	vapour pressure (Pa)
P_0	Coefficient in the Tait state law (Pa)
T	time (s)
T_{ref}	L_{ref}/U_{ref} = reference time (s)
U_{ref}	reference velocity = inlet flow velocity (m/s)
V	control volume (m^3)
α	local void fraction (dimensionless)
μ	dynamic laminar viscosity (Pa.s)
μ_t	dynamic turbulent viscosity (Pa.s)
ρ	$\alpha\rho_v + (1 - \alpha)\rho_l$ local density of the mixture (kg/m^3)
ρ_v	vapour density (kg/m^3)

ρ_l liquid density (kg/m^3)
σ $(P_{ref} - P_{vap})/1/2\rho_l U_{ref}^2$ cavitation number (dimensionless)
σ_{num} numerical cavitation number (dimensionless)
σ_{exp} experimental cavitation number (dimensionless)
$\mathbf{U}$ mixture velocity: 2D vector, of component (u_x, u_y) in the Cartesian orthonormal fixed frame, or (u, v) in the local frame associated with the curvilinear orthogonal mesh (m/s, m/s)

ACKNOWLEDGEMENTS

The authors express their gratitude to the French Space Agency (CNES) for its continuing support.

REFERENCES

1. Reboud JL, Stutz B, Coutier O. Two phase flow structure of cavitation: experiment and modelling of unsteady effects. *3rd International Symposium on Cavitation*, Grenoble, France, 1998.
2. Kueny JL, Schultz F, Desclaud J. Numerical prediction of partial cavitation in pumps and inducers. *IAHR Symposium*, Trondheim, 1988.
3. Kinnas SA, Fine NE. A numerical non-linear analysis of the flow around two and three dimensional partially cavitating hydrofoils. *Journal of Fluid Mechanics* 1993; **254**:151–181.
4. Von Kaenel A, Maitre T, Rebattet C, Kueny JL, Morel P. Three dimensional partial cavitating flow in a rocket turbopump inducer: numerical predictions compared with laser velocimetry measurements. *Cav'95 International Symposium*, Deauville, France, 1995.
5. Peallat JM, Pellone C. Experimental validation of two and three dimensional numerical analysis of partially cavitating hydrofoils. *Journal of Ship Research* 1996; **40**(3):211–223.
6. Furness RA, Hutton SP. Experimental and theoretical studies of two-dimensional fixed-type cavities. *Journal of Fluid Engineering* 1975; **97**:515–522.
7. De Lange DF, De Bruin GJ, Van Winjngaarden L. On the mechanism of cloud cavitation: experiment and modeling. *The Second International Symposium on Cavitation*, April 1994, Tokyo, Japan, 1994.
8. Delannoy Y, Kueny JL. Two phase flow approach in unsteady cavitation modelling. *Cavitation and Multiphase Flow Forum*, *ASME-FED*, vol. 98. 1990; 153–158.
9. Merkle CL, Feng J, Buelow PEO. Computational modelling of the dynamics of sheet cavitation. *3rd International Symposium on Cavitation*, Grenoble, France, 1998.
10. Song C, He J. Numerical simulation of cavitating flows by single-phase flow approach. *3rd International Symposium on Cavitation*, Grenoble, France, April 1998.
11. Kubota A, Kato H, Yamaguchi H. A new modelling of cavitating flows: a numerical study of unsteady cavitation on a hydrofoil section. *Journal of Fluid Mechanics* 1992; **240**:59–96.
12. Chen Y, Heister SD. Modeling hydrodynamic non-equilibrium in bubbly and cavitating flows. *Journal of Fluid Engineering* 1995; **118**(1):172–178.
13. Grogger HA, Alajbegovic A. Calculation of the cavitating flow in venturi geometries using two fluid model. *ASME Paper*, FEDSM99-7364, 1998.
14. Kunz R, Boger D, Chyczewski T, Stinebring D, Gibeling H. Multi-phase CFD analysis of natural and ventilated cavitation about submerged bodies. *3rd ASME/JSME Joint Fluids Engineering Conference*, San Francisco, 1999.
15. Turkel E. Preconditioning methods for solving the incompressible and low speed compressible equations. *Journal of Computational Physics* 1987; **72**:277–298.
16. Patankar SV. *Numerical Heat Transfer and Fluid Flow*. Hemisphere Publishing Corporation, 1981.
17. Reboud JL, Delannoy Y. Two-phase flow modelling of unsteady cavitation. *2nd International Symposium on Cavitation*, Tokyo, 1994.
18. Coutier-Delgosha O, Reboud JL, Albano G. Numerical simulation of the unsteady Cavitation behaviour of an inducer blade cascade. *ASME FEDSM00*, Proceedings, 2000.
19. Stutz B, Reboud JL. Experiments on unsteady cavitation. *Experiments in Fluids* 1997; **23**:191–198.
20. Stutz B, Reboud JL. Two-phase flow structure of sheet cavitation. *Physics of Fluids* 1997; **9**(12):3678–3686.
21. Ishii M. *Thermo-Fluid Dynamic Theory of Two-Phase Flow*. Eyrolles, Paris, 1975.
22. Knapp RT, Daily JT, Hammit FG. *Cavitation*. Mc Graw Hill: New York, 1970.
23. Jakobsen JK. On the mechanism of head breakdown in cavitating inducers. *Journal of Basic Engineering*, *Transactions of the ASME*, June 1964; 291–305.

24. Ryskin G, Leal LG. Orthogonal mapping. *Journal of Computational Physics* 1983; **50**:71–100.
25. Delannoy Y. Modélisation d'écoulements instationnaires et cavitants. *Ph.D. Thesis*, INPG, Grenoble, 1989.
26. Pope SB. The calculation of turbulent recirculating flow in general orthogonal co-ordinates. *Journal of Computational Physics* 1978; **26**:197.
27. Zhu J. A low diffusive and oscillation-free convection scheme. *Communications in Applied Numerical Methods* 1991; **7**:225–232.
28. Orszag SA, *et al. Renormalization Group Modelling and Turbulence Simulations*, *Near Wall Turbulent Flows*. Elsevier: Amsterdam, The Netherlands, 1993.
29. Wilcox D. *Turbulence Modeling for CFD*. DCW Industries, Inc.: La Canada, CA, USA, 1988.
30. Coutier-Delgosha O, Fortes-Patella R, Reboud JL. Evaluation of the turbulence model influence on the numerical simulations of unsteady cavitation. *Journal of Fluid Engineering* 2002; **125**:38–45.
31. Choi D, Merkle CL. The application of preconditioning in viscous flows. *Journal of Computational Physics* 1993; **105**:207–223.
32. Hoeijmakers HWM, Jansens ME, Kwan W. Numerical simulation of sheet cavitation. *CAV98 Third Int. Symposium on Cavitation*, Grenoble, France, 7–10 April 1998.
33. Longatte F. Contribution à l'analyse phénoménologique des écoulements instationnaires dans les turbomachines: Etude du couplage Pompe-circuit et rotor-stator, *Ph.D. Thesis*, Institut National Polytechnique de Grenoble, France, 1998.
34. Kueny J-L, Reboud J-L, Desclaud J. Analysis of partial cavitation: image processing and numerical prediction, ASME-FED Vol. 116, 1991, pp. 55–60.
35. Stutz B. Analyse de la structure diphasique et instationnaire des poches de cavitation, *Ph.D. Thesis*, Institut National Polytechnique de Grenoble, France, 1996.

